HASSAN, I., PETERSON, R. C. & GRUNDY, H. D. (1985). *Acta Cryst.* C**41**, 827–832.
HEATHMAN, S. (1981). *Users Guide and Manual for the Powder Diffractometer D1A*, 1st ed. Institut Laue–Langevin, Grenoble, France.
HEWAT, A. W. (1973). *Fortran IV Version of Rietveld Profile Refinement Program, Modified for Anisotropic Thermal Vibrations*. Internal Rep. No. RRL 73/239. AERE Harwell, England.
HOFMANN, U., HERZENSTIEL, E., SCHOENEMANN, E. & SCHWARZ, K. H. (1969). *Z. Anorg. Allg. Chem.* **367**, 119–129.
JAEGER, F. M. (1929). *Trans. Faraday Soc.* **25**, 320–345.
JAEGER, F. M. & VAN MELLE, F. A. (1929). *Proc. Acad. Sci. Amsterdam*, **32**, 156*ff*.
KLINOWSKI, J., CARR, S. W., TARLING, S. E. & BARNES, P. (1987). *Nature (London)*, **330**, 56–58.
KOESTER, L. & YELON, W. B. (1982). *Summary of Low Energy Neutron Scattering Lengths and Cross Sections*. ECN, Netherlands Energy Research Foundation, Petten, The Netherlands.
KONDO, R. (1965). *Yogyo Kyokai Shi*, **71**, 1–8.
LESCHEWSKI, L. (1935). *Z. Angew. Chem.* **48**, 533–536.
LOEWENSTEIN, W. (1953). *Am. Mineral.* **39**, 92–96.
MORTON, J. R. (1969). *Proc. 15th Colloque Ampère (At. Mol. Etud. Radio Elec.)*, Grenoble, September 1968, pp. 299–303. Amsterdam, London: North Holland.
MULLER, D., HOEBBEL, D. & GESSNER, W. (1981). *Chem. Phys. Lett.* **84**, 25.
ORDER, R. B. VAN & HILL, R. H. (1950). Patent No. 2,806,802. United States Patent Office.
PAULING, L. (1930). *Z. Kristallogr.* **74**, 213–225.
PODSCHUS, E., HOFMANN, U. & LESCHEWSKI, K. (1936). *Z. Anorg. Allg. Chem.* **228**, 305–333.
PRENER, J. S. & WARD, R. (1950). *J. Am. Chem. Soc.* **72**, 2780–2781.
RIETVELD, H. M. (1966). *Acta Cryst.* **20**, 508–513.
RIETVELD, H. M. (1967). *Acta Cryst.* **22**, 151–152.
RIETVELD, H. M. (1969). *J. Appl. Cryst.* **2**, 65–71.
SAALFELD, H. & DEPMEIER, W. (1972). *Krist. Tech.* **7**, 229–233.
SEEL, F. & GUETTLER, H.-J. (1973). *Angew. Chem.* **85**, 416–417.
SEEL, F., GUETTLER, H.-J., SIMON, G. & WIECKOWSKI, A. (1977). *Pure Appl. Chem.* **49**, 45–54.
SEEL, F., GUETTLER, H.-J., WIECKOWSKI, A. & WOLF, B. (1979). *Z. Naturforsch. Teil B*, **34**, 1671–1677.
TARLING, S. E. (1986). *A Crystallographic Investigation of the Structure and Formation of Ultramarine*. PhD Thesis, Univ. of London, England.
TARLING, S. E., BARNES, P. & MACKAY, A. L. (1984). *J. Appl. Cryst.* **17**, 96–99.
THOMPSON, D. V. JR (1933). *The Craftsman's Handbook*, pp. 33–37. New Haven Press.
WYART, J., BARIAND, P. & FILIPPI, J. (1972). *Rev. Geogr. Phys. Geol. Dyn.* **14**, 443–447.
YOUNG, R. A., PRINCE, E. & SPARKS, R. A. (1982). *J. Appl. Cryst.* **15**, 357–359.

Acta Cryst. (1988). B**44**, 135–142

Microstructure of Chain Silicates Investigated by HRTEM

BY M. A. GRIBELYUK AND N. D. ZAKHAROV

Institute of Crystallography, Academy of Sciences of the USSR, Leninski prospekt 59, 117333 *Moscow, USSR*

R. HILLEBRAND

Institute of Solid State Physics and Electron Microscopy, Academy of Sciences of the GDR, Weinberg 2, 4010 *Halle (Saale), German Democratic Republic*

AND T. A. MAKAROVA

Institute of Silicate Chemistry, Academy of Sciences of the USSR, Makarova 2, 199034 *Leningrad, USSR*

(*Received* 4 *February* 1987; *accepted* 28 *October* 1987)

Abstract

A number of sodium chain silicates have been studied by high-resolution transmission electron microscopy, where the second cation, cobalt, has been partially or fully substituted by nickel. Optimum conditions for electron microscope observation of (100) and (101) structure projections as well as of chain-width disorder regions were determined on the basis of computer simulation. The vacancies in the octahedral sites were detected in all samples and their types determined. It has been shown that tetrahedral sites may be occupied in the structure, the cation valence changing correspondingly. Several kinds of ordering of these interstitials were observed in a sample with cobalt partially substituted by nickel. Inclusions of sheet silicates of talc type as well as formation of a 3×1 cation vacancy superlattice in a sheet silicate structure were found in Ni-containing samples.

1. Introduction

Wide-chain pyriboles cover all members of a homologous series with the general stoichiometric formula $M_{n-1}P$. Here M and P indicate mica- and pyroxene-type slabs, having structure formulae $AM_3T_4O_{10}(OH)_2$ and $M_4T_4O_{12}$, where $A = A$ site, $T =$ tetrahedral sites, $M =$ octahedral sites, $n =$ the width of the chain. The progress in their structure determination, particularly

0108-7681/88/020135-08$03.00

© 1988 International Union of Crystallography

defects contained in them, is mainly connected with HRTEM development. The observations on natural minerals have made it possible to detect ordered wide-chain pyriboles that were previously unknown. Thus, small domains of a triple-chain analogue of diopside and tremolite, whose size was insufficient for single-crystal X-ray analysis, were found in nephrite (Jefferson, Mallinson, Hutchinson & Thomas, 1978). On the other hand, chain-width disorder – the irregular alteration of chains of different width – was observed in some cases (Hutchison, Irusteta & Whittaker, 1975; Veblen & Buseck, 1979, 1980). The maximum chain width, as observed in anthophyllite (Veblen & Buseck, 1979), was greater than 300 which corresponds to a continuous transformation of chain silicates into sheet silicates. The chain width also changes along the **c** ('chain termination' defects) and **a** ('zipper termination' defects) axes. Chain terminations, as have been found in nephrite and anthophyllite (Veblen & Buseck, 1980; Veblen & Burnham, 1977), can occur at low-angle grain boundaries as well as a result of cooperative termination of chains in two or more (010) lamellae. Simple and cooperative zipper terminations were observed in *c*-axis images, and termination rules were suggested in order to determine whether the termination is coherent or not. Chain and zipper terminations correspond to those kinds of defects that accompany polysomatic reactions in these materials. Some stages of these reactions were observed in natural silicates (Veblen & Buseck, 1980, 1981; Veblen & Burnham, 1978).

These results show possible types of defects that may occur in chain pyriboles. However, a clear understanding of the nature of such defects needs a comparison with synthesis conditions. This dependence would enable one to judge, by the distortions observed, the processes taking place in the earth's crust during the synthesis. The only possible way to solve this problem is to synthesize wide-chain silicates under controlled conditions and to investigate defects in them. Here we report on the defects in sodium triple-chain silicates studied by HRTEM. A number of different compositions were synthesized where the second cation, cobalt, was partly or fully replaced by nickel. Initial results concerning Na–Co triple-chain silicates have been reported earlier (Zakharov, Khadzhi & Rozhanski, 1979).

2. Experimental

2.1. *Synthesis*

Asbestiform crystals were synthesized under hydrothermal conditions: $T = 623$–773 K and $P > 3 \times 10^7$ Pa in the alkali medium. In the system NaOH–NiO–SiO_2–H_2O(NaCl), chemicals such as $NiCl_2$, NaOH and amorphous SiO_2 were mixed in the bulk composition of the Na–Ni triple-chain silicate $Na_2Ni_4Si_6O_{16}(OH)_2$. In the system NaOH–CoO–SiO_2–H_2O(Na_2SO_4), $CoSO_4$ and $NaSiO_3$ were mixed by coprecipitation in the bulk composition of the Na–Co triple-chain silicate $Na_2Co_4Si_6O_{16}(OH)_2$. In the system NaOH–(NiO–CoO)–SiO_2–H_2O(NaCl), $NiCl_2$, $CoCl_2$, SiO_2 and NaOH were mixed in the bulk composition of the Na–Co(Ni) triple-chain silicate $Na_2Co_2Ni_2Si_6O_{16}(OH)_2$. An excess of sodium alkali was used in all reaction mixtures (about 0·5–5·0wt%). Each of the mixtures was exposed to hydrothermal treatment during 48 h at about $T = 773$ K in a platinum crucible. Asbestiform mixtures of Na–Ni silicate (light green), Na–Co silicate (pink) and Na–Co(Ni) silicate (grey–lilac) were obtained. It should be noted that the temperature for Na–Co silicate formation ($T = 623$ K) is less than that for the Ni-containing silicates ($T = 723$ K).

2.2. *Structure and electron microscopy (EM)*

The fibres of silicate investigated were supported on a holey carbon film and observed in JEM 100C and JEM 200CX electron microscopes under accelerating voltages of 100 and 200 kV, respectively. The objective aperture size was set to $R = 3{\cdot}3$ nm^{-1} in the former case and to $R = 4{\cdot}0$ nm^{-1} in the latter. We faced serious difficulties in preparing the samples in the *c*-axis orientation, therefore only *a*-axis images were recorded.

The triple-chain Na–Co silicate structure corresponds to the monoclinic space group $C2/c$ with the lattice parameters $a = 1{\cdot}0$, $b = 2{\cdot}71$, $c = 0{\cdot}525$ nm, $\beta = 109{\cdot}5°$. Three silicate subchains, joined by tetrahedral vertices, form a sheet in which all the tetrahedra

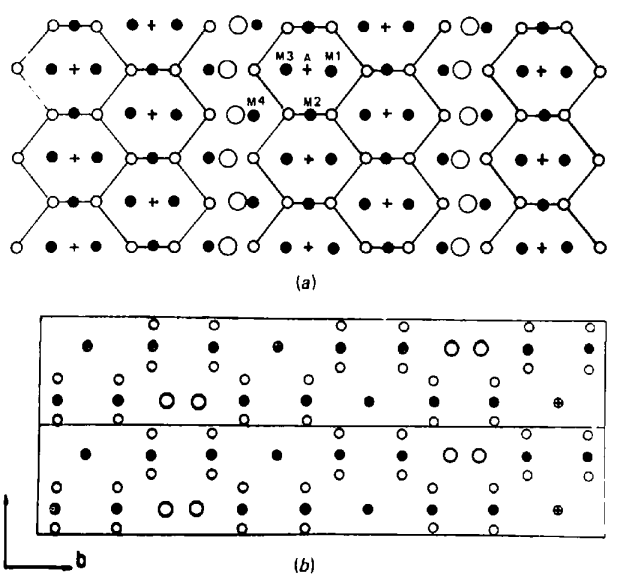

Fig. 1. Structural model of the triple-chain Na–Co silicate: (*a*) (100) projection, (*b*) (101) projection. Only cation positions are indicated: ○, Na; •, Co; ◦, Si; +, *A* site.

have the same orientation. Two such sheets facing back to back make up a triple chain (Fig. 1*a*). The neighbouring triple chains in the [010] direction join together in the same way, as in amphiboles, but the M_5 position is occupied by sodium here. In octahedral sites M_1–M_4, Co^{2+} cations of ionic radius $r_{ion} = 0{\cdot}078$ nm are situated. The problem concerning the A-site occupation by sodium has been discussed on the basis of Na–Mg triple-chain silicate structure analysis (Drits, Goncharov, Aleksandrova, Khadzhi & Dmitrik, 1974; Tateyama, Shimoda & Sudo, 1978), but has remained open.

A multislice procedure was utilized for bright-field-image interpretation (Goodman & Moodie, 1974). All reflections with the reciprocal lattice vectors $|g| \leq 40\ \text{nm}^{-1}$ were used. In order to account for the absorption phenomenon an imaginary part of atomic scattering amplitude $f(g)$ was introduced in the following way: $f_i'(g)/f_i(g) = m_i$ for all g reflections. Here $f_i'(g)$ is the imaginary part of the atomic scattering amplitude for the ith atom and $m_i = 0{\cdot}01 f_i(0)$ for all types of atoms. Effects of incident-beam divergence and chromatic aberration were taken into consideration according to Fejes (1977). The unit cell was divided into three slices along the beam direction. For structure defect image simulation in (100) projection, an artificial unit cell doubled in the c direction was used.

3. Results

3.1. *Computer simulation of EM images in* (100) *and* (101) *structure projections*

A map of 100 kV bright-field calculated images of the Na–Co triple-chain silicate in (100) projection is shown in Fig. 2. Parameters of the EM transfer function corresponded to those of JEM 100C, the objective aperture size R being $3{\cdot}3\ \text{nm}^{-1}$. The most obvious correspondence between the image and the structure projection is observed with a crystal thickness $t \leq 12$ nm, the underfocus being $\Delta f = -70$ to -90 nm. The contrast inside the triple chain reverses in the latter case within the range $t < 12$ nm; therefore, $\Delta f = -70$ to -90 nm is the only optimum range for observation. Bright spots correspond here to the position of hexagonal channels in the structure and bright vertical bands to the boundary between triple chains. Remarkable contrast variations occur in the image sequentially at $\Delta f = -50$, 30 and 80 nm. A further increase of the crystal thickness leads to the appearance of additional details in the image, which hamper its interpretation. For example, incorrect conclusions can be drawn from the image, recorded at $\Delta f = 10$ nm and $t = 24$ nm. Here the triple chain itself and its boundary look almost identical although they are formed by different groups of atoms.

The structure image presented in Fig. 3 shows a good agreement with the calculated one recorded at $\Delta f = -70$ to -90 nm.

The maximum specimen tilt for modern instruments is about 60°. This enables EM images to be recorded both in (100) and (101) projections, because the angle ξ between them is about 30°. The (101) structure projection (Fig. 1*b*) can also be presented as consisting of triple chains, but the neighbouring ones are not shifted by $\mathbf{c}/2$ with respect to each other, as takes place

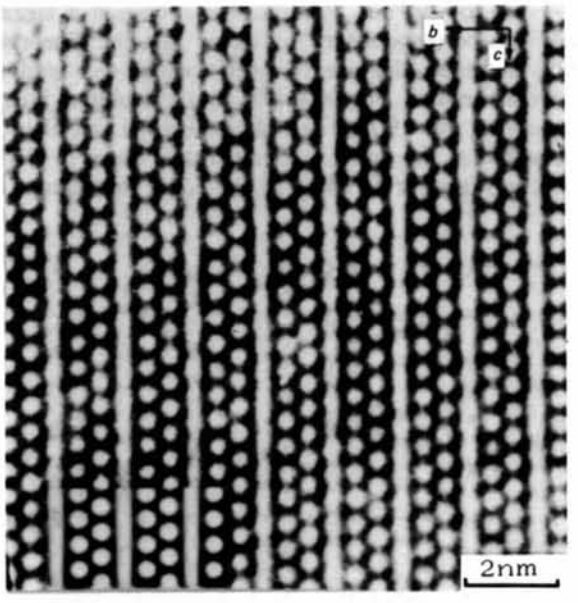

Fig. 3. The theoretical and experimental 100 kV a-axis images of the Na–Co silicate.

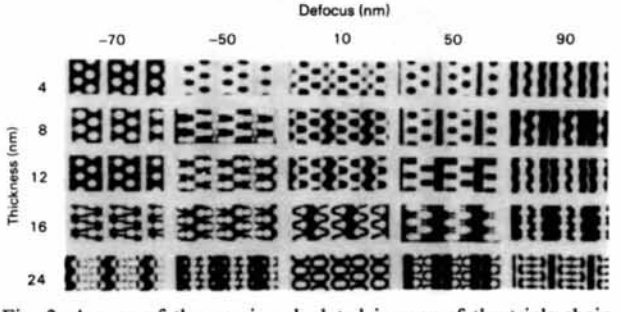

Fig. 2. A map of the a-axis calculated images of the triple-chain Na–Co silicate.

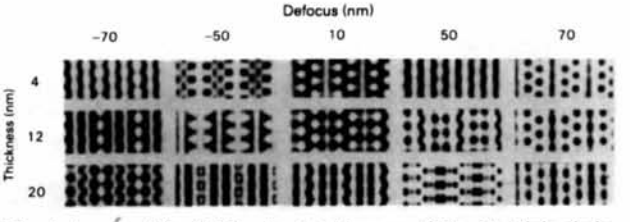

Fig. 4. A map of the (101) calculated images of Na–Co triple-chain silicate.

in (100) projection. The most obvious correlation between the image and structure projection is achieved at $\Delta f = -70$ to -90 and 70–90 nm ($t < 12$ nm, Fig. 4). Bright spots in the image ($\Delta f < 0$) correspond to the position of channels in the structure. Two sodium cations occupy channels at the boundary and a pair of Co and Na cations each occupy a channel in the triple chain (Fig. 1*b*). Therefore bright spots look dimmer in the latter case. Dark spots in the image of a triple chain ($\Delta f > 0$) lie between channels. As in the previous case, one can hardly interpret images recorded at $t > 12$ nm.

3.2. *Chain-width disorder*

Lamellae containing one, four and five subchains have been observed in all investigated samples. Therefore it was necessary to make sure that their images recorded under optimum conditions can be interpreted unambiguously. For these purposes computer simulation of a single pyroxene lamella, incorporated in the triple-chain Na–Co silicate structure was performed (Fig. 5).

Our results show that images of chain-width disorder regions can be readily interpreted at $t < 16$ nm, $\Delta f = -70$ to -90 nm. For the model chosen a zigzag dark line corresponds to pyroxene lamella. Theoretically, however, the use of overfocusing can lead to incorrect results. For example, the calculated image recorded at $\Delta f = 90$ nm ($t = 4$ nm, Fig. 6) can also be interpreted as the image of a quadruple chain in (101) projection (see for comparison the upper right image in Fig. 4). In this case the contrast in the image of a triple chain depends on the width of the neighbouring chain (*cf.* Figs. 2, 6).

The (100) structure image of a pyroxene lamella, incorporated in the triple-chain structure, shows a good correlation with that calculated at $\Delta f = -70$ nm (Fig. 7).

3.3. *Point defects and their ordering*

Considerable changes in the intensity of bright spots in (100) bright-field images recorded under optimum conditions have been also observed (Fig. 8, arrows 1,2). As has been mentioned above, bright spots correspond to hexagonal channels formed by Co^{2+} cations and $(SiO_4)^{4-}$ tetrahedra in structure projection. An additional cation, placed in the channel, lowers the corresponding bright-spot intensity in the image. The problem of *A*-site occupation by Na cations in Na–Mg triple-chain silicates has been investigated by Drits, Goncharov, Aleksandrova, Khadzhi & Dmitrik (1974) and Tateyama, Shimoda & Sudo (1978), but the authors of these papers arrived at opposite conclusions. Therefore, it was reasonable to check whether the contrast changes in Fig. 8 could be explained by the statistical occupation of *A* sites. If so, the bright and dim spots in the image would correspond to channels with fully occupied or fully vacant *A* sites. Fig. 10(*a*) presents the calculated image, where *A* sites in all channels are vacant excluding one channel with fully occupied *A* sites. The contrast $C = (I_{def} - I_{id})/I_{id}$, where I_{def} and I_{id} are the 'defect' and 'ideal' spot intensities, changes within $C = 20$–30% in the range $\Delta f = -70$ to -90 nm. The C value remains constant until $t < 4$ nm, but then sharply increases. The contrast shows that the

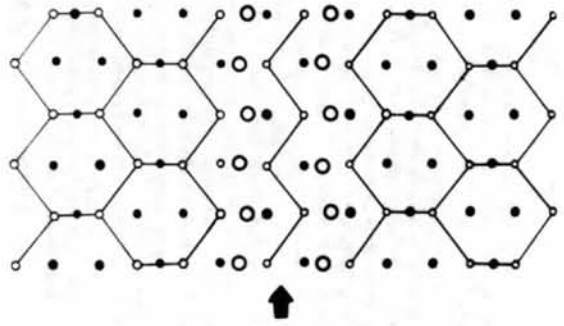

Fig. 5. Pyroxene lamella in the triple-chain structure (arrowed). For atom designations see Fig. 1.

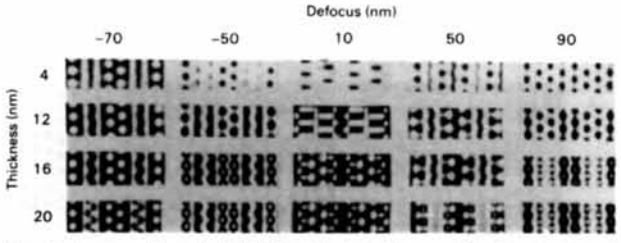

Fig. 6. A map of *a*-axis 100 kV calculated images for the structural model shown in Fig. 5.

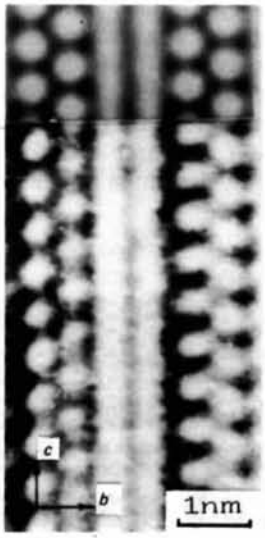

Fig. 7. The theoretical and experimental *a*-axis 100 kV images of the pyroxene lamella incorporated in the triple-chain structure.

crystal thickness $t \leq 8$ nm. A comparison of theoretical and experimental images leads to a conclusion that only small variations in bright-spot intensity can be explained by the statistical occupation of A sites (arrow 1 in Fig. 8, for example).

A more reliable explanation follows from octahedral Co^{2+} sublattice examination (Fig. 9). A sublattice presents a strip where neighbouring octahedra share edges. One can distinguish T_1–T_8 tetrahedral sites that are vacant in the ideal structure. The neighbouring tetrahedra share edges too, but have an opposite orientation: with vertices 'up' and 'down'. The occurrence of very dim spots in the image (Fig. 8, arrow 2) can be explained if one admits that a Co cation displays variable valence in Na–Co silicates. This feature manifests itself in the occupation of tetrahedral sites by the Co^{3+} cation (Clyde Day & Selbin, 1969). The degree of darkening of a triple chain is mainly affected by T_1, T_2, T_7 and T_8 site occupation, and that of T_3 and T_6 sites defines mainly the size and the intensity of bright spots in the image. Fig. 10(*b*) presents the calculated image of a triple chain having fully occupied T_3, T_6 sites in one channel. A crystal thickness of about 4 nm was supposed in this case. Small changes in bright-spot intensity (Fig. 8, arrow 1) can be also explained by a partial occupation of T_3, T_6 sites. As follows from Fig. 8 the tetrahedral site occupation is statistical in nature in Na–Co triple-chain silicates.

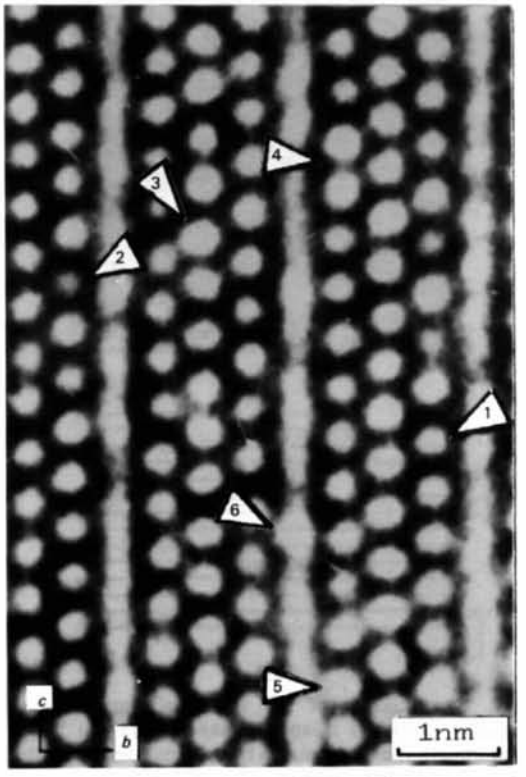

Fig. 8. The *a*-axis 100 kV image of point defects (arrowed).

On the other hand, several kinds of ordering have been observed in Na–Co(Ni) samples. In this case, owing to the value of their ionic radii, Co^{3+} and Ni^{3+} may occupy the T_1–T_8 sites. A quadruple chain looks much darker than the neighbouring triple chain; this may be rationalized in terms of T_1, T_2, T_7 and T_8 site occupation (Fig. 16). This conclusion is confirmed qualitatively by calculation (Fig. 11), where a full occupation of these sites has been supposed. Bright spots in the calculated image of a quadruple chain with occupied sites look dimmer than those in the neighbouring chains. This effect is not observed in the experimental image probably as a result of a partial occupation of these sites. It should be emphasized that the contrast discussed here has been observed only in quadruple chain images.

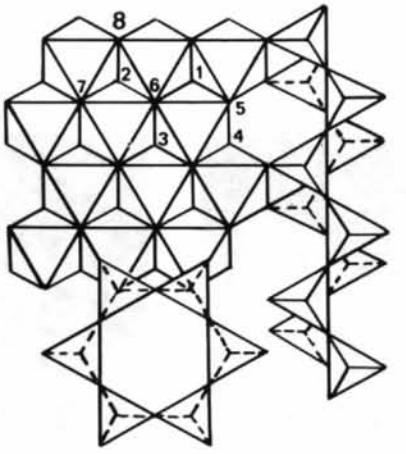

Fig. 9. The octahedral Co sublattice viewed in the [100] direction. Numerals 1–8 indicate tetrahedral sites T_1–T_8.

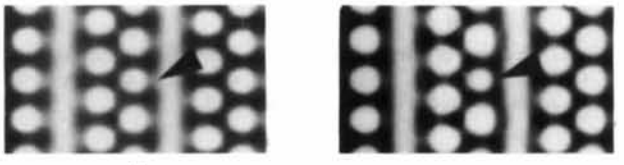

(*a*) (*b*)

Fig. 10. The calculated images of a 'defect' column formed by (*a*) Na cations occupying A sites and (*b*) Co cations occupying T_3, T_6 sites in the channel. The position of the 'defect' column in the image is arrowed.

Fig. 11. The *a*-axis calculated image of a triple chain where all the T_1, T_2, T_7 and T_8 sites are occupied by Co. The crystal thickness $t = 4$ nm.

The chains of dim spots arranged in the c direction have been observed in the triple-chain and sheet structures (Fig. 12). Dim spots correspond to channels with occupied T_3, T_6 sites in a sheet silicate. A more complex pattern is observed in the triple-chain silicate: dim spots in the chain are somewhat shifted in c direction from the position of channel centres (see Fig. 1*a*). Tetrahedral sites, having only one of the two possible orientations in the sublattice, are probably occupied in this case.

Fig. 8 shows also anomalous bright spots (arrow 3), bright vertical lines between spots (arrow 4) and some contrast irregularities at the chain boundary (arrows 5,6). All these features provide evidence for the presence of vacancies (V) in octahedral sites. The theoretical image analysis (Fig. 13) has permitted us to interpret this contrast as the images of Co^{2+} vacancies in M_2 (arrow 4), M_3 (arrow 5) and M_4 (arrow 6) sites. Through-focus series of these defects, obtained at $t = 8$ nm, have enabled us to determine the $C = f(\Delta f, t)$ dependence. The C value depends only slightly on defocus Δf in the range $\Delta f = -70$ to -90 nm in V_{M_3} and V_{M_4} images. Furthermore, C varies with t for V_{M_3} and remains constant with increasing of t for V_{M_4} ($C = 10\%$). Each M_3, M_4 position has been assumed to be vacant in the 'defect' column in calculations. An M_2 vacancy is imaged by a vertical line between bright spots and $\Delta f = -70$ to -80 nm is the optimum defocus value. The C value increases greatly with crystal thickness: from $C = 12\%$ ($t = 2$ nm) to $C = 100\%$ ($t = 8$ nm). All the C values were obtained by averaging over 10 pixels in the [010] direction. It was found that the vertical line between spots can be observed only if at least 60% of all M_2 sites are vacant in the 'defect' column.

The contrast in Fig. 8 arises only in the case when several vacancies are contained in the 'defect' column. The number of defects observed is greater than that predicted solely by a statistical distribution of vacancies. Therefore, formation of vacancy chains may be preferable in terms of the total energy. As can be seen from Fig. 13 all types of Co vacancies produce

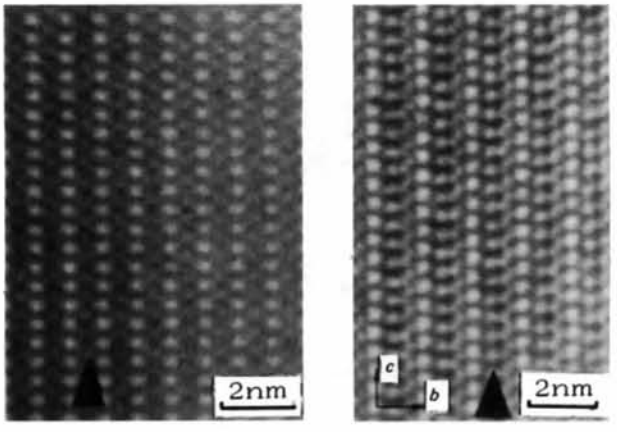

Fig. 12. Ordering of interstitials (*a*) in the sheet silicate and (*b*) in the triple-chain silicate. Chains of faint spots that correspond to channels with occupied T sites are arrowed.

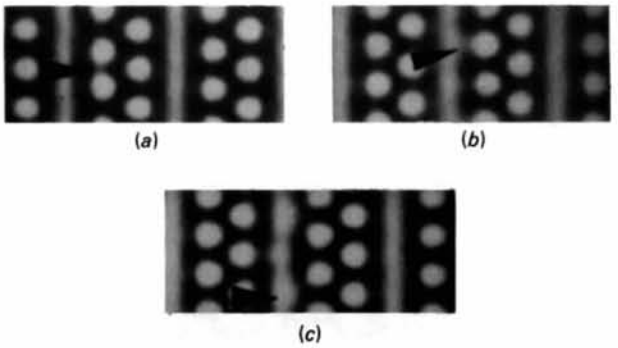

Fig. 13. The calulated images of Co vacancies in M_2 (*a*), M_3 (*b*) and M_4 (*c*) positions. Crystal thickness $t = 4$ nm, all the sites in the 'defect' column are vacant.

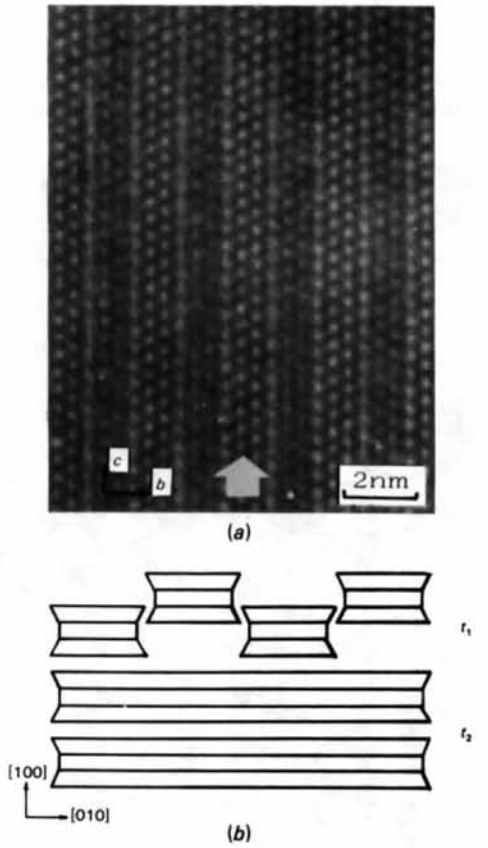

Fig. 14. Superposition of the triple-chain and sheet silicate structures (thickness t_1 and t_2, respectively). (*a*) The 100 kV *a*-axis image. The arrow marks the regions where the channels in the two structures coincide when the structures are superimposed. (*b*) Structural model viewed along the *c* axis.

discernable contrast in the image, which makes it possible to determine the vacancy type from its image.

Thus, our data demonstrate that vacancies in octahedral sites as well as interstitials in tetrahedral sites are present in the octahedral sublattice. This disorder shows that the system is in a nonequilibrium state.

3.4. *Polysomatic reactions*

As has been found in the relevant studies, sheet silicates are an intermediate product of the hydrothermal synthesis of Na–Mg triple-chain silicates. The obvious similarity between this structure and the one investigated suggests that the process occurs in the same way. In agreement with the synthesis conditions, the presence of sheet silicates was detected only in the Ni-containing samples. An *a*-axis image is shown in Fig. 14(*a*), where a triple-chain silicate structure is imposed on a sheet silicate (a very wide chain). A corresponding structure model in *c*-axis projection is shown in Fig. 14(*b*). The lengths of the *b* axes of both structures differ approximately by a factor of 3; therefore, channels are brought to coincidence by imposition in one triple chain and shifting by **c**/2 with respect to each other in the neighbouring ones. In the first case a typical triple-chain image is observed (arrowed); obviously, in the second case the contrast depends on the ratio of the crystal thicknesses of both structures. This ratio was determined for the image shown in Fig. 14(*a*) by the image-matching technique (Fig. 15). $t_1 = 2$ nm and $\Delta f = -100$ nm were used in calculations. As can be seen, the ratio $t_2/t_1 = 2{\cdot}5$ corresponds to the experimental image.

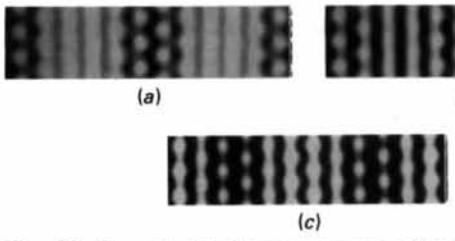

Fig. 15. The calculated images corresponding to the structural model shown in Fig. 14(*a*) for the following $x = t_2/t_1$ values: (*a*) $x = 1$, (*b*) $x = 2$, (*c*) $x = 2{\cdot}5$.

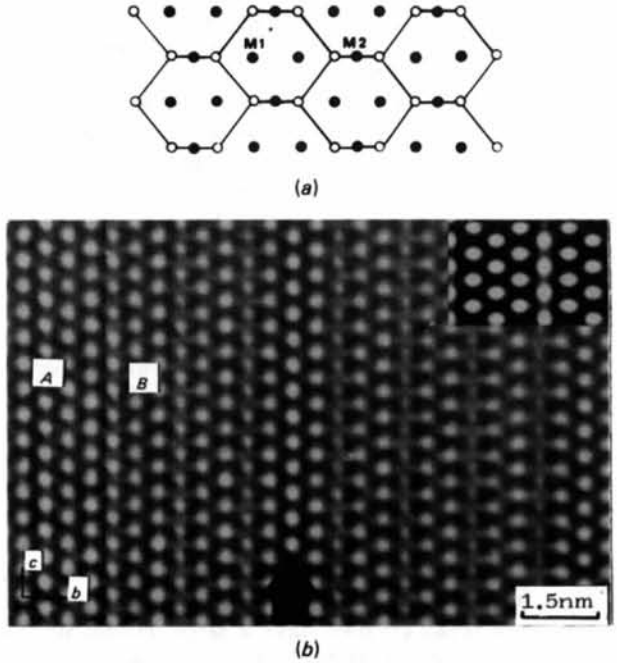

Fig. 16. (*a*) Sheet-silicate structural model. See Fig. 1 for atom designation. (*b*) The 200 kV *a*-axis image of a sheet silicate (*A*) and of the 3 × 1 superlattice of vacancies in M_2 position (*B*). Inset – the calculated image. The dark quadruple chain is arrowed.

An *a*-axis image presented in Fig. 16(*b*) reveals some details of the structure transformation of sheet silicate into the triple-chain silicate. Bright spots in the image of the sheet silicate (area *A*) correspond to channels in the structure projection (Fig. 16*a*). The 3 × 1 superlattice of M_2 vacancies, which is confirmed by image calculations, is observed in this structure (area *B*). The crystal thickness increases from *A* to *B*. The neighbouring subchains in a sheet silicate should be shifted by (**a** + **c**)/2 with respect to each other in order to form bonds, analogous to those in pyroxenes. For this purpose Co^{2+} cations should first be removed from M_2 positions between subchains. Therefore, formation of the V_{M_2} superlattice is a necessary stage of phase transformation. Probably an anomalously dark quadruple chain appears in the image owing to the ordering of Co(Ni) cations, which became excessive during phase transformation.

The presence of sheet silicates in Ni-containing samples can be explained in two ways. A sheet silicate could form as a by-product during the synthesis, or the triple-chain structure synthesis failed to proceed to completion, because the temperature for Na–Co silicates is less than that for Ni-containing silicates. Further studies are required to solve this problem.

The authors are very indebted to Professors N. A. Kiselev, V. N. Rozhanski and J. Heydenreich for valuable discussions. We are also grateful to M. A. Golosova as well to Drs O. A. Kolchin and E. V. Orlova for technical assistance and provision of the program package for output of simulated images to the grey-level display.

References

Clyde Day, M. J. R. & Selbin, J. (1969). *Teoreticheskaja Neorganicheskaja Khimiya*, pp. 1–424. Moscow: Khimiya.

DRITS, V. A., GONCHAROV, Y. I., ALEKSANDROVA, V. A., KHADZHI, I. P. & DMITRIK, A. L. (1974). *Kristallografiya*, **19**, 1186–1193.
FEJES, P. L. (1977). *Acta Cryst.* A**33**, 109–113.
GOODMAN, P. & MOODIE, A. F. (1974). *Acta Cryst.* A**30**, 280–290.
HUTCHISON, J. L., IRUSTETA, M. C. & WHITTAKER, E. J. W. (1975). *Acta Cryst.* A**31**, 794–801.
JEFFERSON, D. A., MALLINSON, L. G., HUTCHISON, J. L. & THOMAS, J. M. (1978). *Contrib. Mineral. Petrol.* **66**, 1–4.
TATEYAMA, H., SHIMODA, S. & SUDO, T. (1978). *Contrib. Mineral. Petrol.* **66**, 149–159.
VEBLEN, D. R. & BURNHAM, C. W. (1977). *Science*, **198**, 359–365.
VEBLEN, D. R. & BURNHAM, C. W. (1978). *Am. Mineral.* **63**, 1053–1073.
VEBLEN, D. R. & BUSECK, P. R. (1979). *Am. Mineral.* **64**, 687–700.
VEBLEN, D. R. & BUSECK, P. R. (1980). *Am. Mineral.* **65**, 599–623.
VEBLEN, D. R. & BUSECK, P. R. (1981). *Am. Mineral.* **66**, 1107–1134.
ZAKHAROV, N. D., KHADZHI, I. P. & ROZHANSKI, V. N. (1979). *Dokl. Akad. Nauk SSSR*, **249**, 359–362.

Acta Cryst. (1988). B**44**, 142–146

Crystal Structure Determination of an Organometallic Compound from Synchrotron Radiation Laue Diffraction Photographs

BY MARJORIE M. HARDING AND S. J. MAGINN

Department of Inorganic, Physical and Industrial Chemistry, Liverpool University, PO Box 147, *Liverpool L*69 3*BX, England*

AND J. W. CAMPBELL, I. CLIFTON AND PELLA MACHIN

*SERC Daresbury Laboratory, Warrington WA*4 4*AD, England*

(*Received* 5 *August* 1987; *accepted* 23 *November* 1987)

Abstract

Laue diffraction patterns for a small single crystal of the organometallic compound [FeRhCl$(CO)_5$dppee] [dppee is $Ph_2PCH(=CH_2)PPh_2$] were recorded with the SRS wiggler beam at SERC Daresbury Laboratory. The intensities were measured from these photographs and the structure determined by Patterson and Fourier methods. The crystal had previously given weak Cu $K\alpha$ Weissenberg photographs from which the unit-cell dimensions and space group were determined. The diffraction data did not extend to plane spacings much less than 1·2 Å and the crystals were found to be disordered; refinement with stereochemical restraints gave $R = 0{\cdot}14$. This is a pilot study; the technique could have uses for very small crystals or for 'kinetic crystallography'. The crystals of [FeRhCl$(C_{26}H_{22}P_2)(CO)_5$], $M_r = 730{\cdot}7$, are monoclinic, $a = 8{\cdot}26$, $b = 19{\cdot}81$, $c = 9{\cdot}77$ Å, $\beta = 111{\cdot}3\ (2)°$ (e.s.d. of ratio of cell edges *ca* 0·1% from Laue diffraction pattern fitting, e.s.d. of absolute values *ca* 1% from weak, low-resolution Weissenberg photograph), $U = 1489{\cdot}5$ Å^3, $F(000) = 732$, space group $P2_1$ or $P2_1/m$ from systematic absences (in Weissenberg photograph, not accessible from Laue), $Z = 2$, D_m (flotation) = 1·62, $D_x = 1{\cdot}63$ g cm^{-3}. The molecule has an Fe–Rh bond, 2·7 Å, and a bridging diphosphine group.

Introduction

Laue diffraction patterns can be recorded with the full 'white' beam of the SRS wiggler at SERC Daresbury Laboratory. Recently programs and procedures have been developed at Daresbury for the measurement of intensities in these Laue photographs, both for proteins and for simpler compounds (Campbell *et al.*, 1988; Helliwell, Machin & Papiz, 1987). The exposure times are remarkably short, 1 s or less for a normal-sized crystal, and a large proportion of reciprocal space can be recorded in a few photographs. Our interest has been to use these procedures for single-crystal structure determination for very small crystals, *e.g.* 5–50 μm dimensions, too small for study with conventional sources, and for which before the development of synchrotron radiation (SR) sources, the only available approach was powder diffraction. Wood, Thompson & Matthewman (1983) have also reported a smaller pilot study in which SR Laue photographs were measured and an attempt was made to refine the parameters of an already known structure (of a normal-sized crystal). Recently the use of the Enraf–Nonius FAST area-detector diffractometer on the wiggler beamline, workstation 9.6 at Daresbury has allowed single-crystal monochromatic intensity data collection and structure determination for a very small crystal of an organic silicate (dimensions 18 × 8 × 175 μm^3) (Andrews *et al.*, 1988). It is apparent from this and other studies that many very small crystals have a large mosaic spread (Andrews, Hails, Harding & Cruickshank, 1987) or other evidence of poor ordering; this makes the measurement of reflection intensities even more difficult than would be predicted on the basis of the size and scattering power of the crystal.

0108-7681/88/020142-05$03.00
© 1988 International Union of Crystallography